Arch Comput Methods Eng
DOI 10.1007/s11831-013-9092-6

Rapid Simulation of Laser Processing of Discrete Particulate Materials

T.I. Zohdi

Received: 10 April 2013 / Accepted: 10 April 2013

Abstract The objective of this paper is to develop a computational model and corresponding solution algorithm to enable rapid simulation of laser processing and subsequent targeted zonal heating of materials composed of packed, discrete, particles. Because of the complex microstructure, containing gaps and interfaces, this type of system is extremely difficult to simulate using continuum-based methods, such as the Finite Difference Time Domain Method or the Finite Element Method. The computationally-amenable model that is developed captures the primary physical events, such as reflection and absorption of optical energy, conversion into heat, thermal conduction through the microstructure and possible phase transformations. Specifically, the features of the computational model are (1) a discretization of a concentrated laser beam into rays, (2) a discrete element representation of the particulate material microstructure and (3) a discrete element transient heat transfer model that accounts for optical (laser) energy propagation (reflection and absorption), its conversion into heat, the subsequent conduction of heat and phase transformations involving possible melting and vaporization. A discrete ray-tracking algorithm is developed, along with an embedded, staggered, iterative solution scheme, which is needed to calculate the optical-to-thermal conversion, particle-to-particle conduction and phase-transformations, implicitly. Numerical examples are given, focusing on concentrated laser beams and the effects of surrounding material conductivity, which draws heat away from the laser contact zone, thus affecting the targeted material state.

T.I. Zohdi
Department of Mechanical Engineering, University of California, Berkeley, CA 94720-1740, USA

1 Introduction: Laser Processing of Particulate Materials

1.1 Motivation

In order to meet the specifications demanded by new products, novel additive manufacturing techniques which involve processing of high-density particle-laden materials, are being developed. Examples include particulate spray coatings, particle-laden ink deposition of printed electronics and compacted particulate powders.[1] Many of these techniques involve laser-driven thermal processing, such as sintering, annealing, melting, drilling, polishing and ablation, which is achieved by melting and vaporization of the discrete particulate materials when they are packed together.

Because of the monochromatic and collimated nature of lasers, they are an attractive way to post-process (anneal, bond, drill, cut, etc.) powdered materials, in particular with beam pulsing. The upper bound for the power of a typical industrial laser is approximately 6000 W. Typically, the initial beam produced is in the form of collimated (parallel) rays that are 1–2 mm apart, which are then focused with a lens onto a small focal point (approximately 50 mm away) of no more than about 0.000025 m in diameter. As the material changes phase from solid to liquid, its absorptivity increases, thus increasing the depth of the cut/hole. While this is the primary way a laser is used in cutting materials, variants include reactive cutting where the laser is used as an ignition source for a flame or thermal stress cracking whereby large thermal gradients are induced causing thermal expansion, stresses and fracture. It is important to note that pulsing the laser (as opposed to a continuous beam) to control the heat

[1] There are a large variety of deposition techniques, and we refer the reader to the surveys of the state of the art found in Martin [32, 33].

Published online: 23 October 2013

affected zone is important when heating the whole piece is undesirable.[2] In summary, because of the extremely tight profit margins and short turn-around times in manufacturing of new materials, there is an industrial need for numerical simulation of laser post-processing of particulate based-materials, in order to reduce and guide time-consuming experiments.

Remark 1 Over fifty percent of the raw materials handled in industry appear in particulate form during the various stages of processing. Consistent, high-quality, particles for manufacturing processes can be produced in a variety of ways, such as: (a) sublimation from a raw solid to a gas, which condenses into particles that are recaptured (harvested), (b) atomization of liquid streams into droplets by breaking jets of metal, (c) reduction of metal oxides and (d) comminution/pulverizing of bulk material.

Remark 2 There has been a huge increase in the use of print-based manufacturing using particle-laden inks, which require rapid laser-induced curing, particularly for printed electronics applications on flexible foundational substrates, such as flexible solar cells and smart electronics. Towards the end of this paper, more applications will be discussed in these emerging areas.

1.2 A Qualitative Descriptions of Laser Processing

In order to make somewhat coarse, qualitative, estimates of the strength of a laser needed to induce a specified temperature change, consider a single lumped mass model for a sample of material shown in Fig. 1 (inside the dashed lines), between two temperature controlled walls. We consider a constant energy input (absorbed irradiance, I^{abs} per unit area) and conduction at the two walls, given by a heat flux $Q = 2\frac{\mathbb{K}A^c}{L}(\theta_w - \theta)$, yielding

$$mC\dot{\theta} = I^{abs}A^b + 2\frac{\mathbb{K}A^c}{L}(\theta_w - \theta), \tag{1.1}$$

where $\mathbb{K}$ is the conductivity, A^b is the area of the beam, A^c is the effective contact area, L is a length-scale parameter for conduction, θ is the sample's temperature and θ_w is the wall temperature. The solution is $(\theta(t=0) = \theta_w)$

$$\theta(t) = \theta_w + \frac{I^{abs}A^bL}{2\mathbb{K}A^c}\big(1 - e^{-\frac{2\mathbb{K}A^ct}{mCL}}\big). \tag{1.2}$$

Two extreme cases are:

- Highly conductive walls (surroundings to the target zone): $\mathbb{K} \to \infty$, $\theta(t) = \theta_w$, where the conductive losses are instantaneous. This will draw heat away from the targeted processing zone.

[2] In addition, there can be possible concerns with overheating the laser device itself.

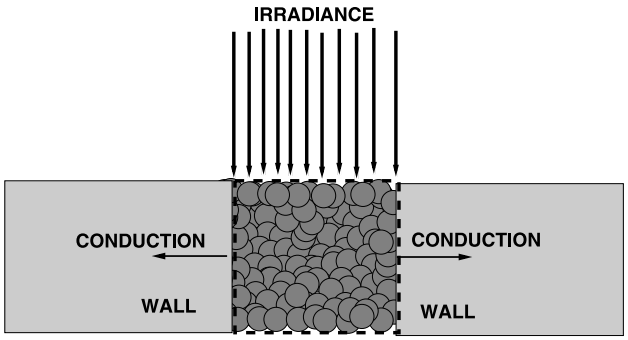

Fig. 1 A laser pulse applied to a plug of material

- Poorly conductive walls (surroundings to the target zone): $\mathbb{K} \to 0$, $\theta(t) = \theta_w + \frac{I^{abs}A^bt}{mC}$, where the conductive losses are zero. This will trap (maximize) heat in the targeted processing zone.

Our goal is to develop a computational tool by assembling relatively simple, physically meaningful, models directly at the particle-scale, for many interacting particles, in order to allow for much more refined estimates of the resulting overall system temperature and, ultimately, its change of phase from a solid, to a liquid to a gas. This will help guide the proper selection of the laser intensity, duration, etc.

1.3 Objectives of This Work

This work develops a computational model and corresponding solution algorithm for the rapid simulation of the laser processing and targeted localized heating of materials composed of discrete particles that are packed together. Such materials possess a complex microstructure which contains gaps and interfaces. This type of process is extremely difficult to simulate using continuum-based methods, such as the Finite Difference Time Domain Method or the Finite Element Method. The model (components of which are shown in Fig. 2) that is developed captures the main physical effects. The features of the computational model are (1) a discretization of a concentrated laser beam into rays, (2) a discrete element representation of the particulate material microstructure and (3) a discrete element transient heat transfer model that accounts for optical (laser) energy propagation (reflection and absorption), its conversion of into heat, the subsequent conduction of heat and phase transformations, involving melting and vaporization. A discrete ray-tracking algorithm is developed, along with an embedded, staggered, iterative solution scheme, in order to calculate the optical-to-thermal conversion, particle-to-particle conduction and phase-transformations, implicitly. Numerical examples are provided to illustrate the model and algorithm.

Remarks The characterization of the flow of concentrated high-frequency energy, the irradiance, through compacted

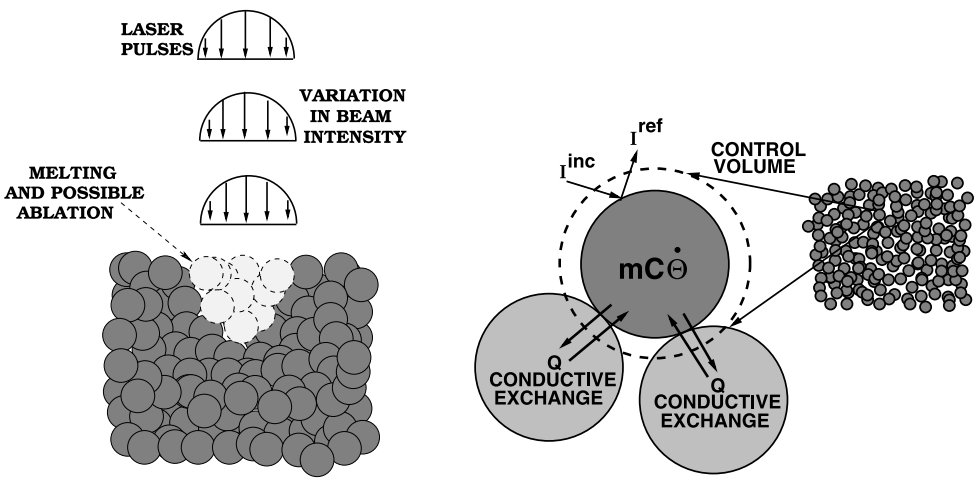

Fig. 2 *Left*: A laser pulse applied to a powdered material. *Right*: Control volume for heat transfer, with an incident ray that encounters an idealized smooth particle scatterer

particulate systems is a key objective of this work. It is assumed that the particles and surface features are at least an order of magnitude larger than the wavelength of the incident electromagnetic radiation, therefore "geometrical" ray tracing theory is applicable, and is well-suited for the systems of interest.

2 Propagation of Electromagnetic Energy

The interest here is on behavior of initially coherent beams (Fig. 2), composed of multiple collinear (collimated) rays (initially forming a planar wave front), where each ray is a vector in the direction of the flow of electromagnetic energy (the rays are parallel to the initial wave's propagation vector). Ray-tracing is a method that is employed to produce rapid approximate solutions to wave-equations for high-frequency/small-wavelength applications where the primary interest is in the overall propagation of energy.[3] Essentially, ray-tracing methods proceed by initially representing wave fronts by an array of discrete rays. *Thereafter, the problem becomes one of an primarily geometric character*, where one tracks the changing trajectories and magnitudes of individual rays which are dictated by the reflectivity and the Fresnel conditions (if a ray encounters a material interface). Ray-tracing methods are well-suited for computation of scattering in complex systems that are difficult to mesh/discretize, relative to procedures such as the Finite Difference Time Domain Method or the Finite Element Method and, therefore, they are frequently employed by analysts in such situations. For review of the state-of-the-art in industrially-oriented optics, see Gross [22]. The next section characterizes ray propagation through particulate media, building on approaches found in Zohdi [50–52].

[3]Resolving diffraction (which ray theory is incapable of describing) is unimportant for the applications of interest.

2.1 Electromagnetic Wave Propagation

The propagation of electromagnetic waves in free space can be described by a simplified form of Maxwell's equations

$$\nabla \times \boldsymbol{E} = -\mu_o \frac{\partial \boldsymbol{H}}{\partial t} \quad \text{and} \quad \nabla \times \boldsymbol{H} = \epsilon_o \frac{\partial \boldsymbol{E}}{\partial t}, \tag{2.1}$$

where $\nabla \cdot \boldsymbol{H} = 0$, $\nabla \cdot \boldsymbol{E} = 0$, $\boldsymbol{E}$ is the electric field intensity, $\boldsymbol{H}$ is the magnetic flux intensity, ϵ_o is the free space permittivity and μ_o is the free space permeability. Using standard vector identities, one can show that

$$\begin{aligned} &\nabla \times (\nabla \times \boldsymbol{E}) = -\mu_o \epsilon_o \frac{\partial^2 \boldsymbol{E}}{\partial t^2} \quad \text{and} \\ &\nabla \times (\nabla \times \boldsymbol{H}) = -\mu_o \epsilon_o \frac{\partial^2 \boldsymbol{H}}{\partial t^2}, \end{aligned} \tag{2.2}$$

and that

$$\nabla^2 \boldsymbol{E} = \frac{1}{c^2} \frac{\partial^2 \boldsymbol{E}}{\partial t^2} \quad \text{and} \quad \nabla^2 \boldsymbol{H} = \frac{1}{c^2} \frac{\partial^2 \boldsymbol{H}}{\partial t^2}, \tag{2.3}$$

where the speed of electromagnetic waves is $c = \frac{1}{\sqrt{\epsilon_o \mu_o}}$. All electromagnetic radiation travels, in a vacuum, at the speed $c \approx 2.99792458 \times 10^8 \pm 1.1$ m/s. In any another medium, for electromagnetic waves, the propagation speed is $v = \frac{1}{\sqrt{\epsilon \mu}}$, where ϵ and μ are the electric permittivity and magnetic permeability of that medium, respectively.[4]

2.2 Plane Harmonic Wave Fronts

Now consider the special case of plane harmonic waves, for example of the form

$$\boldsymbol{E} = \boldsymbol{E}_o \cos(\boldsymbol{k} \cdot \boldsymbol{x} - \omega t) \quad \text{and} \quad \boldsymbol{H} = \boldsymbol{H}_o \cos(\boldsymbol{k} \cdot \boldsymbol{x} - \omega t), \tag{2.4}$$

[4]The free space electric permittivity is $\epsilon_o = \frac{1}{c^2 \mu_o} = 8.8542 \times 10^{-12}\ \mathrm{C\,N^{-1}\,m^{-1}}$ and the free space magnetic permeability is $\mu_o = 4\pi \times 10^{-7}\ \mathrm{Wb\,A^{-1}\,m^{-1}} = 1.2566 \times 10^{-6}\ \mathrm{Wb\,A^{-1}\,m^{-1}}$.

where $\boldsymbol{x}$ is an initial position vector to the wave front, where $\boldsymbol{k}$ is the direction of propagation. For plane waves, $\boldsymbol{k} \cdot \boldsymbol{x} = constant$. We refer to the phase as $\phi = \boldsymbol{k} \cdot \boldsymbol{x} - \omega t$, and $\omega = \frac{2\pi}{\tau}$ as the angular frequency, where τ is the period. For plane waves, the wave front is a plane on which ϕ is constant, which is orthogonal to the direction of propagation, characterized by $\boldsymbol{k}$. In the case of harmonic waves, we have

$$\boldsymbol{k} \times \boldsymbol{E} = \mu_o \omega \boldsymbol{H} \quad \text{and} \quad \boldsymbol{k} \times \boldsymbol{H} = -\epsilon_o \omega \boldsymbol{E}, \tag{2.5}$$

and $\boldsymbol{k} \cdot \boldsymbol{E} = 0$ and $\boldsymbol{k} \cdot \boldsymbol{H} = 0$. The three vectors, $\boldsymbol{k}$, $\boldsymbol{E}$ and $\boldsymbol{H}$ constitute a mutually orthogonal triad.[5] The direction of wave propagation is given by $\frac{\boldsymbol{E} \times \boldsymbol{H}}{\|\boldsymbol{E} \times \boldsymbol{H}\|}$. Electromagnetic waves traveling through space carry electromagnetic energy which flows in the direction of wave propagation. The energy per unit area per unit time flowing perpendicularly into a surface in free space is given by the Poynting vector $\boldsymbol{S} = \boldsymbol{E} \times \boldsymbol{H}$.

2.3 Special Case: Natural (Random) Electromagnetic Energy Propagation

Since at high-frequencies $\boldsymbol{E}$, $\boldsymbol{H}$ and $\boldsymbol{S}$ oscillate rapidly, it is impractical to measure instantaneous values of $\boldsymbol{S}$ directly. Consider the harmonic representations in (2.4) which leads to $\boldsymbol{S} = \boldsymbol{E}_o \times \boldsymbol{H}_o \cos^2(\boldsymbol{k} \cdot \boldsymbol{x} - \omega t)$, and consequently the average value over a longer time interval ($\mathcal{T}$) than the time scale of rapid random oscillation,

$$\langle \boldsymbol{S} \rangle_{\mathcal{T}} = \boldsymbol{E}_o \times \boldsymbol{H}_o \big\langle \cos^2(\boldsymbol{k} \cdot \boldsymbol{x} - \omega t) \big\rangle_{\mathcal{T}} = \frac{1}{2} \boldsymbol{E}_o \times \boldsymbol{H}_o, \tag{2.6}$$

leading to the definition of the *irradiance*

$$I \stackrel{\text{def}}{=} \big\langle \|\boldsymbol{S}\| \big\rangle_{\mathcal{T}} = \frac{1}{2} \|\boldsymbol{E}_o \times \boldsymbol{H}_o\| = \frac{1}{2} \sqrt{\frac{\epsilon_o}{\mu_o}} \|\boldsymbol{E}_o\|^2. \tag{2.7}$$

Thus, the rate of flow of energy is proportional to the square of the amplitude of the electric field. Furthermore, in isotropic media, which we consider for the remainder of the work, the direction of energy is in the direction of $\boldsymbol{S}$ and in the same direction as $\boldsymbol{k}$.

2.4 Beam Decomposition into Rays

The appendix provides more details on the theory of ray representations of electromagnetic waves. Since I is the energy per unit area per unit time, if we multiply by the "cross-sectional" area of the ray (A^r), we obtain the energy associated with an entire beam by multiplying the irradiance by the cross-sectional area of a coherent beam, $I A^b$, where A^b is the cross-sectional area of the beam (comprising all of the rays). The energy for a ray in the beam is then given by $I A^r = I A^b / N_r$, where N_r is the number of rays in the beam (Fig. 3).

[5] By combining the relations in (2.5) one obtains $\|\boldsymbol{k}\| = \frac{\omega}{c}$.

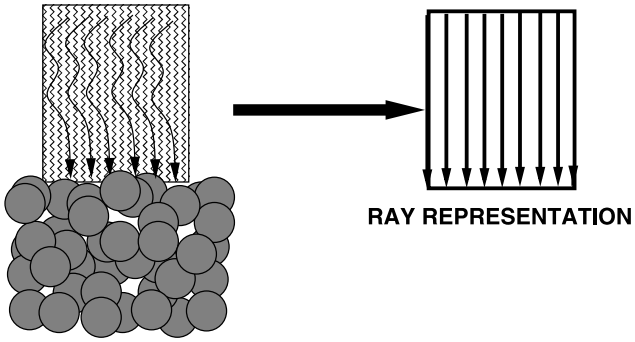

Fig. 3 Decomposition of an incoming beam into idealized "rays"

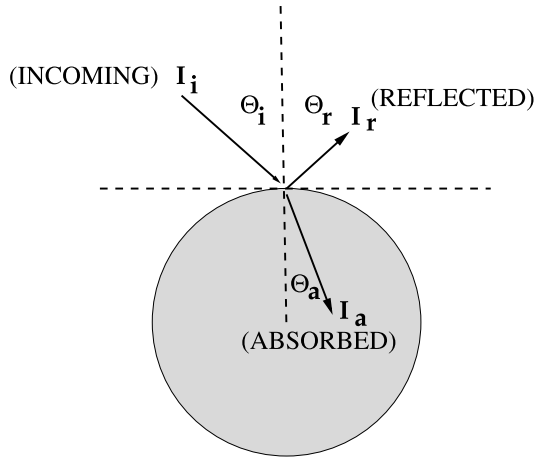

Fig. 4 Reflection and absorption of an incoming ray

The angle between the point of contact of a ray (Fig. 4) and the outward normal to the surface at that point is the angle of incidence (θ_i). The classical reflection law ("Snell's Law") states that the angle at which the ray is reflected is the same as the angle of incidence and that the incoming (incident, θ_i) and outgoing (reflected, θ_r) rays lay in the same plane, and that $\theta_i = \theta_r$. Furthermore, the refraction/absorption law states that, if the ray passes from one medium into a second one (with a different index of refraction) and, if the index of refraction of the second medium is less than that of the first, then the angle the ray makes with the normal to the interface is always less than the angle of incidence, where θ_a is the angle of the absorbed ray (Fig. 4), $n \stackrel{\text{def}}{=} \frac{c}{v} = \sqrt{\frac{\epsilon \mu}{\epsilon_o \mu_o}} = \frac{\sin \theta_i}{\sin \theta_a}$, c is the propagation speed in a vacuum and v is the propagation speed in the incident medium. By using the classical Fresnel equations, one can also describe the changes in ray magnitude. For example if we consider a ray incident upon a boundary separating two different materials, which produces a reflected ray and an absorbed (refracted) ray (Fig. 2), the amount of incident electromagnetic energy (I_i) that is reflected (I_r) is given by the total reflectance $\mathbb{R} \stackrel{\text{def}}{=} \frac{I_r}{I_i}$, where $0 \leq \mathbb{R} \leq 1\text{e}$, $\mathbb{R}$

given by (2.25), for unpolarized electromagnetic radiation, where $\hat{n}$ is the ratio of the refractive indices of the ambient (incident) medium (n_i) and absorbing particle medium (n_a), $\hat{n} = n_a/n_i$, where $\hat{\mu}$ is the ratio of the magnetic permeabilities of the surrounding incident medium (μ_i) and absorbing particle medium (μ_a), $\hat{\mu} = \mu_a/\mu_i$. Although we will present a relatively general formulation, later we will consider applications where the magnetic permeability is, within experimental measurements, virtually the same for both the surroundings and particle. In other words, later in the work, we shall take $\hat{\mu} = 1$ ($\mu_o = \mu_i = \mu_a$) and, thus, $\hat{n} = \frac{n_a}{n_i} = \sqrt{\frac{\epsilon_a \mu_a}{\epsilon_i \mu_i}} \Rightarrow \epsilon_a \mu_a = (\hat{n})^2 \epsilon_i \mu_i \Rightarrow \epsilon_a = (\hat{n})^2 \epsilon_i$, where $\epsilon_i = \epsilon_o$.

Remark Specifically, the regimes of interest are where the particle scatterers and surface features are larger than visible light rays: 3.8×10^{-7} m $\leq \lambda \leq 7.2 \times 10^{-7}$ m. Thus, the particles in this analysis are assumed to possess diameters larger than approximately 10^{-5} m (10 microns). For particulate systems smaller than this, one can simply use the ensuing results as qualitative guides. However, the range of applicability of lasers is not limited to visible frequencies. Other high frequency applications where the developed model can be employed include UV-rays, X-rays, gamma rays and correspondingly smaller particle scatterer sizes, such as (a) regimes where the scatterers and surface features are larger than ultraviolet rays (10^{-9} m $\leq \lambda \leq 10^{-8}$ m), (b) regimes where the scatterers and surface features are larger than X-rays (10^{-11} m $\leq \lambda \leq 10^{-9}$ m), and (c) regimes where the scatterers and surface features are larger than gamma-rays (10^{-12} m $\leq \lambda \leq 10^{-11}$ m).

2.4.1 *Reflection and Absorption of Energy-Fresnel Relations*

We consider a plane harmonic wave incident upon a plane boundary separating two different materials, which produces a reflected wave and an absorbed (refracted) wave (Fig. 2). Two cases for the electric field vector are considered: (1) electric field vectors that are parallel ($\|$) to the plane of incidence and (2) electric field vectors that are perpendicular ($\perp$) to the plane of incidence. In either case, the tangential components of the electric and magnetic fields are required to be continuous across the interface. Consider case (1). We have the following general vectorial representations

$$\begin{aligned} &\boldsymbol{E}_{\|} = E_{\|} \cos(\boldsymbol{k} \cdot \boldsymbol{x} - \omega t) \boldsymbol{e}_1 \quad \text{and} \\ &\boldsymbol{H}_{\|} = H_{\|} \cos(\boldsymbol{k} \cdot \boldsymbol{x} - \omega t) \boldsymbol{e}_2, \end{aligned} \tag{2.8}$$

where $\boldsymbol{e}_1$ and $\boldsymbol{e}_2$ are orthogonal to the propagation direction $\boldsymbol{k}$. By employing the law of refraction ($n_i \sin\theta_i = n_a \sin\theta_a$) we obtain the following conditions relating the incident, reflected and absorbed components of the electric field quantities

$$\begin{aligned} &E_{\|i} \cos\theta_i - E_{\|r} \cos\theta_r = E_{\|a} \cos\theta_a \quad \text{and} \\ &H_{\perp i} + H_{\perp r} = H_{\perp a}. \end{aligned} \tag{2.9}$$

Since, for plane harmonic waves, the magnetic and electric field amplitudes are related by $H = \frac{E}{v\mu}$, we have

$$E_{\|i} + E_{\|r} = \frac{\mu_i}{\mu_a} \frac{v_i}{v_a} E_{\|a} = \frac{\mu_i}{\mu_a} \frac{n_a}{n_i} E_{\|a} \stackrel{\text{def}}{=} \frac{\hat{n}}{\hat{\mu}} E_{\|a}, \tag{2.10}$$

where $\hat{\mu} \stackrel{\text{def}}{=} \frac{\mu_a}{\mu_i}$, $\hat{n} \stackrel{\text{def}}{=} \frac{n_a}{n_i}$ and where v_i, v_r and v_a are the values of the velocity in the incident, reflected and absorbed directions.[6] By again employing the law of refraction, we obtain the Fresnel reflection and transmission coefficients, generalized for the case of unequal magnetic permeabilities

$$\begin{aligned} r_{\|} &= \frac{E_{\|r}}{E_{\|i}} = \frac{\frac{\hat{n}}{\hat{\mu}} \cos\theta_i - \cos\theta_a}{\frac{\hat{n}}{\hat{\mu}} \cos\theta_i + \cos\theta_a} \quad \text{and} \\ a_{\|} &= \frac{E_{\|a}}{E_{\|i}} = \frac{2\cos\theta_i}{\cos\theta_a + \frac{\hat{n}}{\hat{\mu}} \cos\theta_i}. \end{aligned} \tag{2.11}$$

Following the same procedure for case (2), where the components of $\boldsymbol{E}$ are perpendicular to the plane of incidence, we have

$$\begin{aligned} r_{\perp} &= \frac{E_{\perp r}}{E_{\perp i}} = \frac{\cos\theta_i - \frac{\hat{n}}{\hat{\mu}} \cos\theta_a}{\cos\theta_i + \frac{\hat{n}}{\hat{\mu}} \cos\theta_a} \quad \text{and} \\ a_{\perp} &= \frac{E_{\perp a}}{E_{\perp i}} = \frac{2\cos\theta_i}{\cos\theta_i + \frac{\hat{n}}{\hat{\mu}} \cos\theta_a}. \end{aligned} \tag{2.12}$$

Our primary interest is in the reflections. We define the reflectances as

$$\mathbb{R}_{\|} \stackrel{\text{def}}{=} r_{\|}^2 \quad \text{and} \quad \mathbb{R}_{\perp} \stackrel{\text{def}}{=} r_{\perp}^2. \tag{2.13}$$

Particularly convenient forms for the reflections are

$$\begin{aligned} r_{\|} &= \frac{\frac{\hat{n}^2}{\hat{\mu}} \cos\theta_i - (\hat{n}^2 - \sin^2\theta_i)^{\frac{1}{2}}}{\frac{\hat{n}^2}{\hat{\mu}} \cos\theta_i + (\hat{n}^2 - \sin^2\theta_i)^{\frac{1}{2}}} \quad \text{and} \\ r_{\perp} &= \frac{\cos\theta_i - \frac{1}{\hat{\mu}} (\hat{n}^2 - \sin^2\theta_i)^{\frac{1}{2}}}{\cos\theta_i + \frac{1}{\hat{\mu}} (\hat{n}^2 - \sin^2\theta_i)^{\frac{1}{2}}}. \end{aligned} \tag{2.14}$$

Thus, the total energy reflected can be characterized by

$$\mathbb{R} \stackrel{\text{def}}{=} \left(\frac{E_r}{E_i} \right)^2 = \frac{E_{\perp r}^2 + E_{\|r}^2}{E_i^2} = \frac{I_{\|r} + I_{\perp r}}{I_i}. \tag{2.15}$$

If the resultant plane of oscillation of the (polarized) wave makes an angle of γ_i with the plane of incidence, then

$$E_{\|i} = E_i \cos\gamma_i \quad \text{and} \quad E_{\perp i} = E_i \sin\gamma_i, \tag{2.16}$$

[6] Throughout the analysis we assume that $\hat{n} \geq 1$.

and it follows from the previous definition of I that

$$I_{\|i} = I_i \cos^2\gamma_i \quad \text{and} \quad I_{\perp i} = I_i \sin^2\gamma_i. \tag{2.17}$$

Substituting these expression back into the expressions for the reflectances yields

$$\begin{aligned}\mathbb{R} &= \frac{I_{\|r}}{I_i}\cos^2\gamma_i + \frac{I_{\perp r}}{I_i}\sin^2\gamma_i \\ &= \mathbb{R}_{\|}\cos^2\gamma_i + \mathbb{R}_{\perp}\sin^2\gamma_i.\end{aligned} \tag{2.18}$$

For natural or unpolarized electromagnetic radiation, the angle γ_i varies rapidly in a random manner, as does the field amplitude. Thus, since

$$\langle\cos^2\gamma_i(t)\rangle_{\mathcal{T}} = \frac{1}{2} \quad \text{and} \quad \langle\sin^2\gamma_i(t)\rangle_{\mathcal{T}} = \frac{1}{2}, \tag{2.19}$$

and therefore for natural electromagnetic radiation

$$I_{\|i} = \frac{I_i}{2} \quad \text{and} \quad I_{\perp i} = \frac{I_i}{2} \tag{2.20}$$

and therefore

$$r_{\|}^2 = \left(\frac{E_{\|r}^2}{E_{\|i}^2}\right)^2 = \frac{I_{\|r}}{I_{\|i}} \quad \text{and} \quad r_{\perp}^2 = \left(\frac{E_{\perp r}^2}{E_{\perp i}^2}\right)^2 = \frac{I_{\perp r}}{I_{\perp i}}. \tag{2.21}$$

Thus, the total reflectance becomes

$$\mathbb{R} = \frac{1}{2}(\mathbb{R}_{\|} + \mathbb{R}_{\perp}) = \frac{1}{2}\big(r_{\|}^2 + r_{\perp}^2\big), \tag{2.22}$$

where $0 \leq \mathbb{R} \leq 1$. For the cases where $\sin\theta_a = \frac{\sin\theta_i}{\hat{n}} > 1$, one may rewrite reflection relations as

$$\begin{aligned} r_{\|} &= \frac{\frac{\hat{n}^2}{\hat{\mu}}\cos\theta_i - j(\sin^2\theta_i - \hat{n}^2)^{\frac{1}{2}}}{\frac{\hat{n}^2}{\hat{\mu}}\cos\theta_i + j(\sin^2\theta_i - \hat{n}^2)^{\frac{1}{2}}} \quad \text{and} \\ r_{\perp} &= \frac{\cos\theta_i - \frac{1}{\hat{\mu}}j(\sin^2\theta_i - \hat{n}^2)^{\frac{1}{2}}}{\cos\theta_i + \frac{1}{\hat{\mu}}j(\sin^2\theta_i - \hat{n}^2)^{\frac{1}{2}}}, \end{aligned} \tag{2.23}$$

where, $j = \sqrt{-1}$, and in this complex case[7]

$$\mathbb{R}_{\|} \overset{\text{def}}{=} r_{\|}\bar{r}_{\|} = 1 \quad \text{and} \quad \mathbb{R}_{\perp} \overset{\text{def}}{=} r_{\perp}\bar{r}_{\perp} = 1, \tag{2.24}$$

where $\bar{r}_{\|}$ and $\bar{r}_{\perp}$ are complex conjugates. Thus, for angles above the critical angle θ_i^*, all of the energy is reflected. Notice that as $\hat{n} \to 1$ we have complete absorption, while as $\hat{n} \to \infty$ we have complete reflection. The amount of absorbed irradiance by the particles is $I_a = (1 - \mathbb{R})I_i$.

2.4.2 Reflectivity

To observe the dependency of $\mathbb{R}$ on $\hat{n}$ and θ_i we can explicitly write

$$\begin{aligned}\mathbb{R} = \frac{1}{2}\Bigg(&\left(\frac{\frac{\hat{n}^2}{\hat{\mu}}\cos\theta_i - (\hat{n}^2 - \sin^2\theta_i)^{\frac{1}{2}}}{\frac{\hat{n}^2}{\hat{\mu}}\cos\theta_i + (\hat{n}^2 - \sin^2\theta_i)^{\frac{1}{2}}}\right)^2 \\ &+ \left(\frac{\cos\theta_i - \frac{1}{\hat{\mu}}(\hat{n}^2 - \sin^2\theta_i)^{\frac{1}{2}}}{\cos\theta_i + \frac{1}{\hat{\mu}}(\hat{n}^2 - \sin^2\theta_i)^{\frac{1}{2}}}\right)^2\Bigg),\end{aligned} \tag{2.25}$$

[7] The limiting case $\frac{\sin\theta_i^*}{\hat{n}} = 1$, is the critical angle (θ_i^*) case.

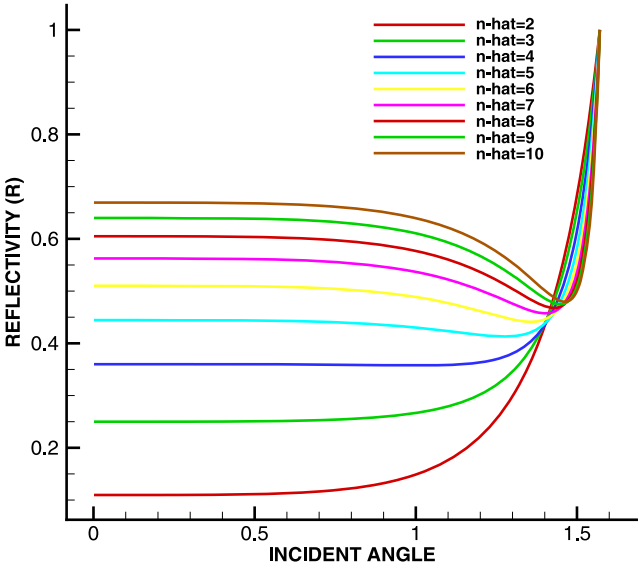

Fig. 5 The reflectance ($\mathbb{R}$) as a function of incident angle

which is plotted in Fig. 5. For all but $\hat{n} > 4$, is there discernible nonmonotone behavior. The nonmonotone behavior is slight for $\hat{n} = 4$, but nonetheless present. Clearly, as $\hat{n} \to \infty$, $\mathbb{R} \to 1$, no matter what the angle of incidence's value. We note that as $\hat{n} \to 1$, provided that $\hat{\mu} = 1$, $\mathbb{R} \to 0$, i.e. all incident energy is absorbed (it is transparent). With increasing $\hat{n}$, the angle for minimum reflectance grows larger. For more details, we refer the reader to the relatively recent treatise of Gross [22] and the cited literature in the references.

Remark 3 From this point forth, we assume that the ambient and interstitial medium (surrounding the particles) behaves as a vacuum. Accordingly, there are no energetic losses as the rays move through the surrounding medium. Furthermore, we assume that absorbed rays that enter a particle are not re-emitted, but are converted into a heat source.

Remark 4 We note that the use of lasers for the related problem of dermal ablation is well-established, and involves the use of special types of dyes to increase absorption of the tissue, referred to as sclerostomics. The dyes are applied by electrophoresis, i.e. electrical current is used to direct dye into tissue. There are five main types of interaction: (1) photochemical, (2) thermal, (3) photoablation, (4) plasma-induced ablation and (5) photodisruption. Photochemical Interaction-stems from empirical observations that light can induce chemical effects and reactions within macromolecules or tissue within macromolecules or tissue. Biostimulation is also attributed to photochemical interaction. Photodynamics therapy is performed as follows: first a photosynthesizer is injected into the tissue. It remains inactive until irradiated. This can be used for targeted interaction. Thermal interaction can be classified as (a) coagulation, (b) vaporization, (c) carbonization

and (d) melting. The probability of cells staying alive depends on the duration and temporal evolution of the temperature obtained. Photoablation-etching was first applied to polymethyl-metacrylate (PMMA), polyimide, Teflon and other synthetic polymers. For more details, see Niemz [35], Steen [48] and Grigoropoulos [21].

3 Thermal Conversion of Beam (Optical) Losses

It is assumed that the particle scatterers are small enough to consider the temperature as being uniform within each particle. Furthermore, we assume that the space between the particle scatterers, i.e. the "ether", plays no role in the heat transfer process. Conduction is assumed to occur between particles in contact. An energy balance governing thermal storage in a particle (i), the absorption of optical energy from rays which come in contact (N_{rc}) and all conductive exchange with other particles in contact (N_{pc}), reads as

$$m_i C_i \dot{\theta}_i = \underbrace{\sum_{j=1}^{N_{pc}} Q_{ij}}_{\text{conduction}} + \underbrace{\sum_{k=1}^{N_{rc}} \mathcal{H}_{ik}^{rays}}_{\text{ray sources}} \stackrel{\text{def}}{=} \mathcal{F}_i^{tot}. \tag{3.1}$$

We remark that the validity of using a lumped thermal model for each particle, i.e. ignoring temperature gradients and assuming a uniform temperature within a particle scatterer, is dictated by the magnitude of the Biot number. A small Biot number (significantly less than unity) indicates that such an approximation is reasonable. The Biot number for spheres scales with the ratio of particle scatterer volume (V) to particle scatterer surface area (A_s), $\frac{V}{A_s} = \frac{\mathcal{R}}{3}$ ($\mathcal{R}$ is the particle radius), which indicates that a uniform temperature distribution is appropriate, since the particle scatterers, by definition, are small. For the conductive contribution, we have[8]

$$\sum_{j=1}^{N_{pc}} \mathcal{Q}_{ij} \approx \sum_{j=1}^{N_{pc}} \mathbb{K}_{ij} A_{ij}^c \frac{\theta_j - \theta_i}{\|\boldsymbol{r}_j - \boldsymbol{r}_i\|} \stackrel{\text{def}}{=} \mathcal{Q}_i^{tot}. \tag{3.2}$$

The energy absorbed by a particle i from a ray in contact ($k = 1, \ldots, N_{pc}$) is defined as

$$\begin{aligned} \Delta \mathcal{H}_i^{rays,tot} &\stackrel{\text{def}}{=} \int_t^{t+\Delta t} \sum_{k=1}^{N_{rc}} \mathcal{H}_{ik}^{rays}\, dt \\ &\approx \sum_{k=1}^{N_{rc}} \left(I_{ik}^{inc} - I_{ik}^{ref}\right) A_r \Delta t \\ &= \sum_{k=1}^{N_{rc}} (1 - \mathbb{R}_{ik}) I_{ik}^{inc} A_r \Delta t, \end{aligned} \tag{3.3}$$

where I^{inc} is the incoming ray's irradiance, I^{ref} is the reflected ray's irradiance, A_r is an ray-area parameter that is computed by taking the total initial cross-sectional area of the entire beam (collimated rays) and dividing it by the total number of rays. *As stated previously, explicitly, the ray-area parameter was calculated as* $A_r \stackrel{\text{def}}{=} A^b/N_r$, *where* N_r *is the number of rays in the beam and* A^b *is the initial cross-sectional area of the beam.*

Remark 5 Convective and infrared radiative effects are considered of secondary importance in the current analysis, but have been accounted for in Zohdi [51] for related applications.

Remark 6 From this point forth, we will denote I^{inc} instead of I_i and I^{ref} instead of I_r to avoid any possible confusion with subscripts to come later.

Remark 7 In order to determine the approximate contact area, referring to Fig. 6, one can solve for an approximation of the contact area radius a_{ij} (and the contact area, $A_{ij}^c = \pi a_{ij}^2$) by solving the following three equations:

$$a_{ij}^2 + L_i^2 = \mathcal{R}_i^2, \tag{3.4}$$

and

$$a_{ij}^2 + L_j^2 = \mathcal{R}_j^2, \tag{3.5}$$

and

$$L_i + L_j = \|\boldsymbol{r}_i - \boldsymbol{r}_j\|, \tag{3.6}$$

where $\mathcal{R}_i$ is the radius of particle i, $\mathcal{R}_j$ is the radius of particle j, L_i is the distance from the center of particle i and the common contact interpenetration line and L_j is the distance from the center of particle j and the common contact interpenetration line. The particle interpenetration is

$$\delta_{ij} = \mathcal{R}_i + \mathcal{R}_j - \|\boldsymbol{r}_i - \boldsymbol{r}_j\|. \tag{3.7}$$

Solving these equations leads to

$$A_{ij}^c = \pi a_{ij}^2 = \pi\left(\mathcal{R}_i^2 - L_i^2\right), \tag{3.8}$$

where

$$L_i = \frac{1}{2}\left(\|\boldsymbol{r}_i - \boldsymbol{r}_j\| - \frac{\mathcal{R}_j^2 - \mathcal{R}_i^2}{\|\boldsymbol{r}_i - \boldsymbol{r}_j\|}\right). \tag{3.9}$$

3.1 Algorithmic Details

After temporal integration with a finite difference time-step of Δt, we have, using a trapezoidal rule with variable ($0 \leq \phi \leq 1$) integration metric:

$$\begin{aligned} &\theta_i(t + \Delta t) \\ &\quad = \theta_i(t) + \frac{1}{m_i C_i} \int_t^{t+\Delta t} \mathcal{F}_i^{tot}\, dt \end{aligned}$$

[8] $\mathbb{K}_{ij}$ is approximated by the average interfacial value of the $i - j$ pair, $\mathbb{K}_{ij} \approx \frac{\mathbb{K}_i + \mathbb{K}_j}{2}$.

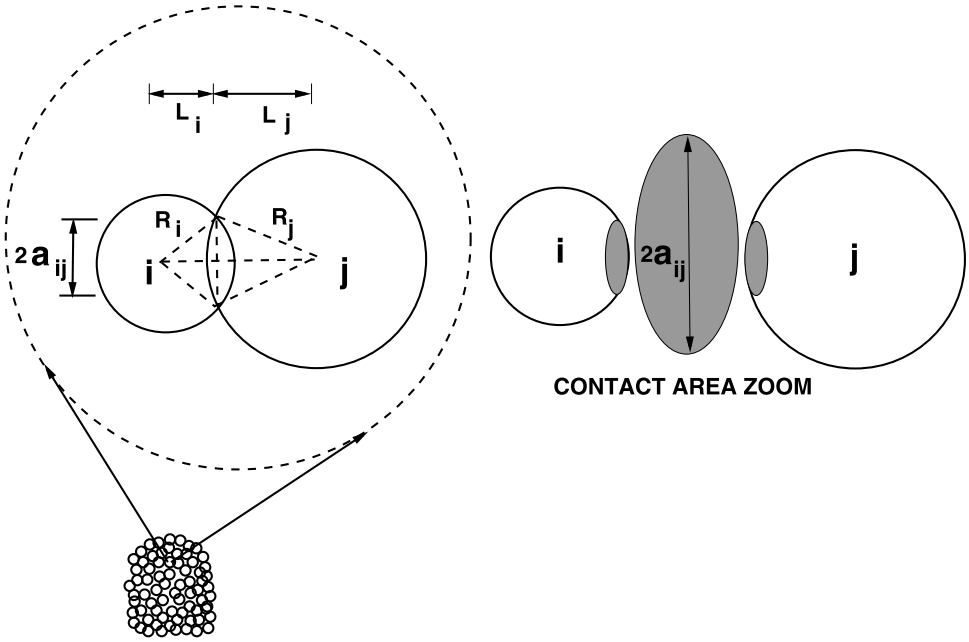

Fig. 6 An approximation of the contact area parameter

$$
\begin{aligned}
&= \theta_i(t) + \frac{1}{m_i C_i}\Bigg(\int_t^{t+\Delta t} \underbrace{\sum_{k=1}^{N_{pc}} \mathcal{Q}_{ik}}_{\mathcal{Q}_i^{tot}}\, dt \\
&\quad + \underbrace{\int_t^{t+\Delta t} \sum_{j=1}^{N_{rc}} \mathcal{H}_{ij}^{rays}\, dt}_{\Delta\mathcal{H}_i^{rays,tot}}\Bigg) \\
&\approx \theta_i(t) + \frac{1}{m_i C_i}\Big(\underbrace{\big(\phi\mathcal{Q}_i^{tot}(t+\Delta t) + (1-\phi)\mathcal{Q}_i^{tot}(t)\big)\Delta t}_{smooth} \\
&\quad + \underbrace{\Delta\mathcal{H}_i^{rays,tot}}_{unsmooth}\Big), \qquad (3.10)
\end{aligned}
$$

where the term "smooth" indicates temporally smoothly varying and "unsmooth" denotes a much shorter discrete event (incident rays encountering and reflecting off of a particle). Thus, explicitly,

$$
\begin{aligned}
&\theta_i^{K+1}(t+\Delta t) \\
&\quad = \theta_i(t) \\
&\qquad + \frac{\Delta t\phi}{m_i C_i}\sum_{j=1}^{N_{pc}} \frac{\mathbb{K}_{ij} A_{ij}^c(\theta_j^K(t+\Delta t) - \theta_i^K(t+\Delta t))}{\|\boldsymbol{r}_j - \boldsymbol{r}_i\|} \\
&\qquad + \frac{\Delta t(1-\phi)}{m_i C_i}\sum_{j=1}^{N_{pc}} \frac{\mathbb{K}_{ij} A_{ij}^c(\theta_j(t) - \theta_i(t))}{\|\boldsymbol{r}_j - \boldsymbol{r}_i\|} \\
&\qquad + \frac{\Delta\mathcal{H}_i^{rays,tot}}{m_i C_i}. \qquad (3.11)
\end{aligned}
$$

This iterative procedure is embedded into the overall ray-tracing scheme. The overall algorithm is as follows, starting at $t = 0$ and ending at $t = T$:

1. COMPUTE NEW RAY MAGNITUDES AND ORIENTATIONS AFTER REFLECTION: I_j^{ref}, $j = 1, 2, \ldots,$ *Rays*.
2. COMPUTE ABSORPTION CONTRIBUTIONS TO THE PARTICLE SCATTERERS: $\Delta\mathcal{H}_i^{rays,tot}$, $i = 1, 2, \ldots,$ *Particles*.
3. COMPUTE CONDUCTION OF THE PARTICLE SCATTERERS: $\mathcal{Q}_i^{tot}$, $i = 1, 2, \ldots,$ *Particles*.
4. COMPUTE PARTICLE TEMPERATURES RECURSIVELY K $= 1, 2, \ldots,$ UNTIL CONVERGENCE, USING EQUATION (3.11) FOR θ_i, $i = 1, 2, \ldots,$ *Particles*, REPEATING STEPS 1–4.
5. INCREMENT ALL RAY POSITIONS: $\boldsymbol{x}_j(t+\Delta t) = \boldsymbol{x}_j(t) + \Delta t\boldsymbol{v}_j(t)$, $j = 1, 2, \ldots,$ *Rays*.
6. INCREMENT TIME ($t = t + \Delta t$), GO TO STEP 1 AND REPEAT STEPS 1–5.

Remark In order to capture all of the ray reflections that occur, the time step size Δt is dictated by the size of the particle scatterers. A somewhat ad-hoc approach is to scale the time step size by the speed of the of ray propagation according to $\Delta t = \xi\frac{\mathcal{R}}{\|\boldsymbol{v}\|}$, where $\mathcal{R}$ is the median radius of the particle scatterers (if the particle sizes are not uniform) and $0.05 \leq \xi \leq 0.1$. Typically, the results are insensitive to ξ that are smaller than this range. The subsequent convergence of the thermal calculation is rather quick, since the time steps are extremely small. For more details on convergence on iterative time-stepping schemes, see Zohdi [53–59].

4 Phase Transformations: *Solid* ⇒ *Liquid* ⇒ *Vapor*

To include phase transformations, we consider five cases, which is implemented in a predictor-corrector manner by first solving

$$m_i C_i \dot{\theta}_i = \mathcal{F}_i^{tot} \tag{4.1}$$

to obtain predicted temperature, and then checking the following:

- *Solid* → *solid-no melting with* $C_i = C_S$: If $\theta(t) < \theta_m$ and $\theta(t+\Delta t) < \theta_m$ then retain (4.1) with $C(\theta) = C_S$,
- *Solid* → *liquid-melting with* $C_i = C_S$: If $\theta(t) < \theta_m$ and $\theta(t+\Delta t) \geq \theta_m$ then re-solve (4.1) with $C(\theta) = C_S + \frac{\delta \mathcal{P}^{S\to L}}{\delta\theta}$,
- *Liquid* → *liquid-melted with* $C_i = C_L$: If $\theta(t) \geq \theta_m$ and $\theta(t+\Delta t) \geq \theta_m$ then retain (4.1) with $C(\theta) = C_L$,
- *Liquid* → *solid-solidification with* $C_i = C_L$: If $\theta(t) \geq \theta_m$ and $\theta(t+\Delta t) < \theta_m$ then re-solve (4.1) with $C(\theta) = C_L + \frac{\delta \mathcal{P}^{L\to S}}{\delta\theta}$,
- *Liquid* → *vapor-vaporization with* $C_i = C_L$: If $\theta(t) < \theta_v$ and $\theta(t+\Delta t) \geq \theta_v$ then re-solve (4.1) with $C(\theta) = C_L + \frac{\delta \mathcal{P}^{L\to V}}{\delta\theta}$,

where C_S is the heat capacity of the solid and C_L is the heat capacity of the liquid and

- $0 < \delta\mathcal{P}^{S\to L}$ is the latent heat of melting,
- $0 < \delta\mathcal{P}^{L\to S}$ is the latent heat of solidification,
- $0 < \delta\mathcal{P}^{L\to V}$ is the latent heat of vaporization,
- $0 < \delta\theta$ is small and can be thought of as a "bandwidth" for a phase transformation. For more details on melting processes, see Davis [9].

Remark 8 Latent heats have a tendency to resist the phase transformations, achieved by adding the positive terms in the denominator, thus enforcing reduced temperature (during the phase transformation).[9] This approach is relatively straightforward to include within the staggering framework.

Remark 9 As a consequence, the number of particles in the system and their heat capacities will also change in the algorithm, and (3.11) becomes

$$\begin{aligned}\theta_i^{K+1}(t+\Delta t) = \theta_i(t) &+ \frac{\Delta t\phi}{m_i C_i^K(t+\Delta t)} \\ &\times \sum_{j=1}^{N_{pc}^K} \frac{\mathbb{K}_{ij} A_{ij}^c (\theta_j^K(t+\Delta t) - \theta_i^K(t+\Delta t))}{\|\boldsymbol{r}_j - \boldsymbol{r}_i\|} \\ &+ \frac{\Delta t(1-\phi)}{m_i C_i(t)} \sum_{j=1}^{N_{pc}} \frac{\mathbb{K}_{ij} A_{ij}^c (\theta_j(t) - \theta_i(t))}{\|\boldsymbol{r}_j - \boldsymbol{r}_i\|} \\ &+ \frac{\Delta \mathcal{H}_i^{rays,tot,K}}{m_i C_i^K(t+\Delta t)}.\end{aligned} \tag{4.2}$$

Remark 10 Vaporized particles are removed from the simulation for subsequent time-steps.

4.1 Optional Time-Scaling and for Simulation Acceleration

Some scaling arguments can be made to accelerate computations. Consider the a system that is subjected to a source $\mathcal{F}(t)$

$$mC\dot{\theta} = \mathcal{F}(t). \tag{4.3}$$

Integrating overall time interval T and breaking it up into M subintervals yields ($\tau = \frac{T}{M}$)

$$\begin{aligned}\theta(T) &= \theta(t=0) + \underbrace{\frac{1}{mC}\int_o^T \mathcal{F}\,dt}_{\text{heat input}} \\ &= \theta(t=0) \\ &\quad + \underbrace{\frac{1}{mC}\left(\int_0^\tau \mathcal{F}\,dt + \int_\tau^{2\tau} \mathcal{F}\,dt + \cdots + \int_{(M-1)\tau}^{M\tau} \mathcal{F}\,dt\right)}_{\text{heat input}}.\end{aligned} \tag{4.4}$$

If $\mathcal{F}(t)$ is periodic over each subinternal $((i-1)\tau, i\tau)$, $i = 1, 2, \ldots, M$, then

$$\begin{aligned}\theta(T) &= \theta(t=0) \\ &\quad + \underbrace{\frac{1}{mC}\left(\int_0^\tau \mathcal{F}\,dt + \int_\tau^{2\tau} \mathcal{F}\,dt + \cdots + \int_{(M-1)\tau}^{M\tau} \mathcal{F}\,dt\right)}_{\text{heat input}} \\ &= \theta(t=0) + \frac{M}{mC}\int_0^\tau \mathcal{F}\,dt \\ &= \theta(t=0) + \underbrace{\frac{1}{(\frac{mC}{M})}}_{pseudo\,thermal\,mass}\int_0^\tau \mathcal{F}\,dt,\end{aligned} \tag{4.5}$$

where the last line is an approximation of the heat input "dumped" into the system. One can interpret $\frac{mC}{M}$ as a pseudo (reduced) thermal mass. Specifically, for the applications of interest here, if absorbed irradiance loading $\Delta\mathcal{H}^{rays,tot}$ was perfectly periodic (repeated over shorter time intervals), with no phase changes (which would change C and the $\Delta\mathcal{H}^{rays,tot}$ absorbed) and if the conductive flux terms were constant (it is not in the general case), then running the simulation over $(0, \tau)$, using $\frac{mC}{M}$ as a pseudo (reduced) thermal mass, would be equivalent to a simulation over the interval

[9] In the idealized limit, the temperature would be constant.

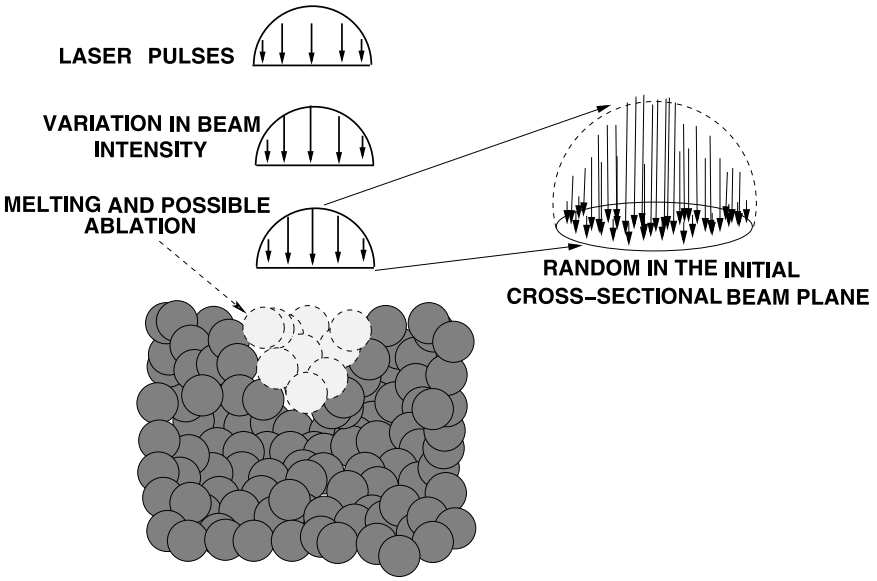

Fig. 7 A laser pulse applied to a plug of material with $N_r = 1000$ parallel, randomly placed rays in the circular cross-sectional plane of the beam, corresponding to unpolarized incoming optical energy

$(0, T)$ using mC. *Thus, as an optional approximation*, either by magnifying I or reducing mC one can deliver the approximate "heat dump", provided one fully resolves the movement of a pulse through the entire system to accurately capture the share of the energy reflected and absorbed by the particles.

Remark In the simple case

$$
\begin{aligned}
&mC\dot{\theta} = \mathcal{F} = IA^b \quad \Rightarrow \\
&\theta(T) = \theta(0) + \frac{IA^bT}{mC} = \theta(0) + M\frac{IA^b\tau}{mC} \\
&\qquad = \theta(0) + \frac{IA^b\tau}{(\frac{mC}{M})},
\end{aligned}
\tag{4.6}
$$

the periodic approximation is exact.

5 Numerical Examples

As a model problem, we considered a group of N_p overlapping randomly packed spherical particles, of equal size, in a cubical domain of dimensions, $D \times D \times D$. The particle size was determined by a particle/sample size ratio, which was defined via a subvolume size $V \stackrel{\text{def}}{=} \frac{D\times D\times D}{N_p}$, where N_p was the number of particles in the entire cubical domain. The non-dimensional ratio between the radius ($\mathcal{R}$) and the subvolume was denoted by $\mathcal{L} \stackrel{\text{def}}{=} \frac{\mathcal{R}}{V^{\frac{1}{3}}}$. If the particles were perfectly arranged in a cubical array, a value of $\mathcal{L} = 0.25$ would mean that they just touch, and values of $\mathcal{L} > 0.25$ would indicate overlapping. Later, in the simulations was used $\mathcal{L} = 0.325$ as an example. We steadily increased the number of rays in the beam from $N_r = 100, 200$, etc. until the results were insensitive to further refinements. This approach indicated that approximately $N_r = 1000$ parallel, but randomly placed, rays in the circular cross-sectional plane of the beam (Fig. 7), corresponding to unpolarized incoming optical energy yielded stable results.[10] Therefore, we consider the responses to be, for all practical purposes, independent of the ray-grid density. This particle/ray system provided convergent results, i.e. increasing the number of rays and/or the number of particles surrounding the beam resulted in negligibly different overall system responses. Of course, there can be cases where much higher resolution may be absolutely necessary.[11] In such a direct numerical approach, one can easily introduce nonuniform beam profiles such as shown in Fig. 2

$$
I(d) = I(d=0)e^{-ad}, \tag{5.1}
$$

where d is the distance from the center of the initial beam line. In the case of $a = 0$ we recapture a flat beam, $I(d) = I(d = 0)$. We specifically used $a = 2$. We set total initial irradiance via $\sum_{i=1}^{N_r} I_i^{inc}(t=0)A_r = 6000$ W.[12] Other simulation parameters of importance were:

- The dimensions of the sample were 10^{-3} m $\times$ 10^{-3} m $\times$ 10^{-3} m.
- The initial velocity vector for all initially collinear rays comprising the beam was $v = (c, 0, 0)$, where $c = 3 \times 10^8$ m/s is the speed of light in a vacuum.

[10] We repeatedly refined the "ray density" up to 10000 rays and found no significant difference compared to the 1000 ray result.

[11] In order to adequately compare between different tests in Table 1, the same random 1000 particle ensemble was used each time.

[12] To achieve this distribution, we first placed rays randomly in the plane, and then scaled the individual I^{inc} by e^{-ad} and the normalized the average so that the total was 6000 W.

- Twenty pulses were applied, allowing each pulse to completely enter and exit the system.
- We used a refractive index ratio of $\hat{n} = 1.4$, for the set of particle scatterers and surrounding environment and enforced a condition that if the material melted, we reduced the refractive index ratio to approximately $\hat{n} = 1$.
- We used a melting temperature of $\theta_m = 600$ Kelvin and a vaporization temperature of $\theta_v = 700$ Kelvin.
- The time-scaling factor, $M = 10^6$.
- The material density, $\rho = 1000\ \text{kg/m}^3$.
- The solid heat capacity, $C_S = 1000\ \text{J/(kg K)}$.
- The liquid heat capacity, $C_L = 2000\ \text{J/(kg K)}$.
- The latent heat of melting, $\frac{\delta \mathcal{P}^{S\to L}}{\delta\theta} = 1000\ \text{J/(kg K)}$.
- The latent heat of solidification, $\frac{\delta \mathcal{P}^{L\to S}}{\delta\theta} = 1000\ \text{J/(kg K)}$.
- The latent heat of vaporization, $\frac{\delta \mathcal{P}^{L\to V}}{\delta\theta} = 1000\ \text{J/(kg K)}$.

We considered a series of numerical experiments starting at $\mathbb{K} = 0$ (no conductivity), where a maximum number of particles were vaporized, until a $\mathbb{K}$ was met where virtually no particles were vaporized during the process. While it is not the objective of this work to carry out a series of parameter studies, we show some trends in Fig. 9 and Table 1. Specifically, Fig. 9 illustrates the volume fraction of particles that are vaporized for increasing $\mathbb{K}$. The final results are tabulated in Table 1. As theoretically predicted, with low $\mathbb{K}$ values, the heat is retained, and virtually all of the particles underneath the beam were vaporized. As $\mathbb{K}$ increases, the heat conducts away from the target zone, and less particles meet the criteria for melting and vaporization. In Fig. 8, starting from left to right and top to bottom, the progressive movement of rays comprising a beam whose initial diameter is 0.3 the length of the sample, as it is being absorbed by the material. We have the following general observations, which are consistent with the analytical results:

- No conductivity retains heat for vaporization-it concentrates the heat in the target zone and more particles are vaporized in a cascading effect because of the reduction of the refractive index, which absorbs more optical energy.
- As the conductivity increases, heat is conducted away from the target zone, and less particles are vaporized.

The utility of the numerical simulation tool is, of course, that one can probe deeper into the spatial evolution of the temperature, phase-changes and vaporization.

Remark The simulations take on the order of two minutes on a laptop. For extremely large-scale systems, it is important to note that for the ray tracing method, there are two natural ways to proceed to exploit parallelism: (1) By assigning each processor its share of the rays, and checking which particle scatterers interact with those rays or (2) By assigning each processor its share of particle scatterers, and checking which rays interact with those particle scatterers. High-performance computational methods for the determination of ray/particle intersection can be developed by slightly modifying fast ray-particle contact detection algorithms found in, for example, Donev et al. [12–16] or Pöschel and Schwager [40], for general particle shapes.

6 Summary and Extensions

This work developed a computational model and a corresponding solution algorithm for the rapid simulation of the laser processing of materials. The objective was to simulate targeted zonal heating of discrete particles that are packed together, in particular focusing on phase transformations and vaporization of particles in the target zone. Because of the complex microstructure, containing gaps and interfaces, this type of system is extremely difficult to simulate using continuum-based methods, such as the Finite Difference Time Domain Method or the Finite Element Method. The model that was developed captured the primary effects, namely, reflection and absorption of optical energy, its conversion into heat via (1) a discretization of a concentrated laser beam into rays, (2) a discrete element representation of the particulate material microstructure and (3) a discrete element transient heat transfer model that accounts for optical (laser) energy propagation (reflection and absorption), its conversion of into heat, the subsequent conduction of heat and phase transformations involving melting and vaporization. A discrete ray-tracking algorithm was developed, along with an embedded, staggered, iterative solution scheme, in order to calculate the optical-to-thermal conversion, particle-to-particle conduction and phase-transformations, implicitly. Current work is focusing on laser treatment of different types of microstructures that arise in other processing methods of particulate materials, such as self-assembly, which leads to very regular patterns that are induced by inserting the particles in solution, depositing them onto surfaces, and evaporating the interstitial liquid, thus allowing hydrodynamic forces to induce the mentioned patterns (Choi et al. [5–7], Demko et al. [10, 11]). Another example where structured media can occur is spray processing of small-scale particles, which can induce chainlike microstructures, due to surface tension and alignment with electrical field lines during deposition (Zohdi [59]). The application of laser processing to these materials is under investigation by the author.[13]

[13] For review of the wide range of particle deposition processes, in particular sprays, see Martin [32, 33].

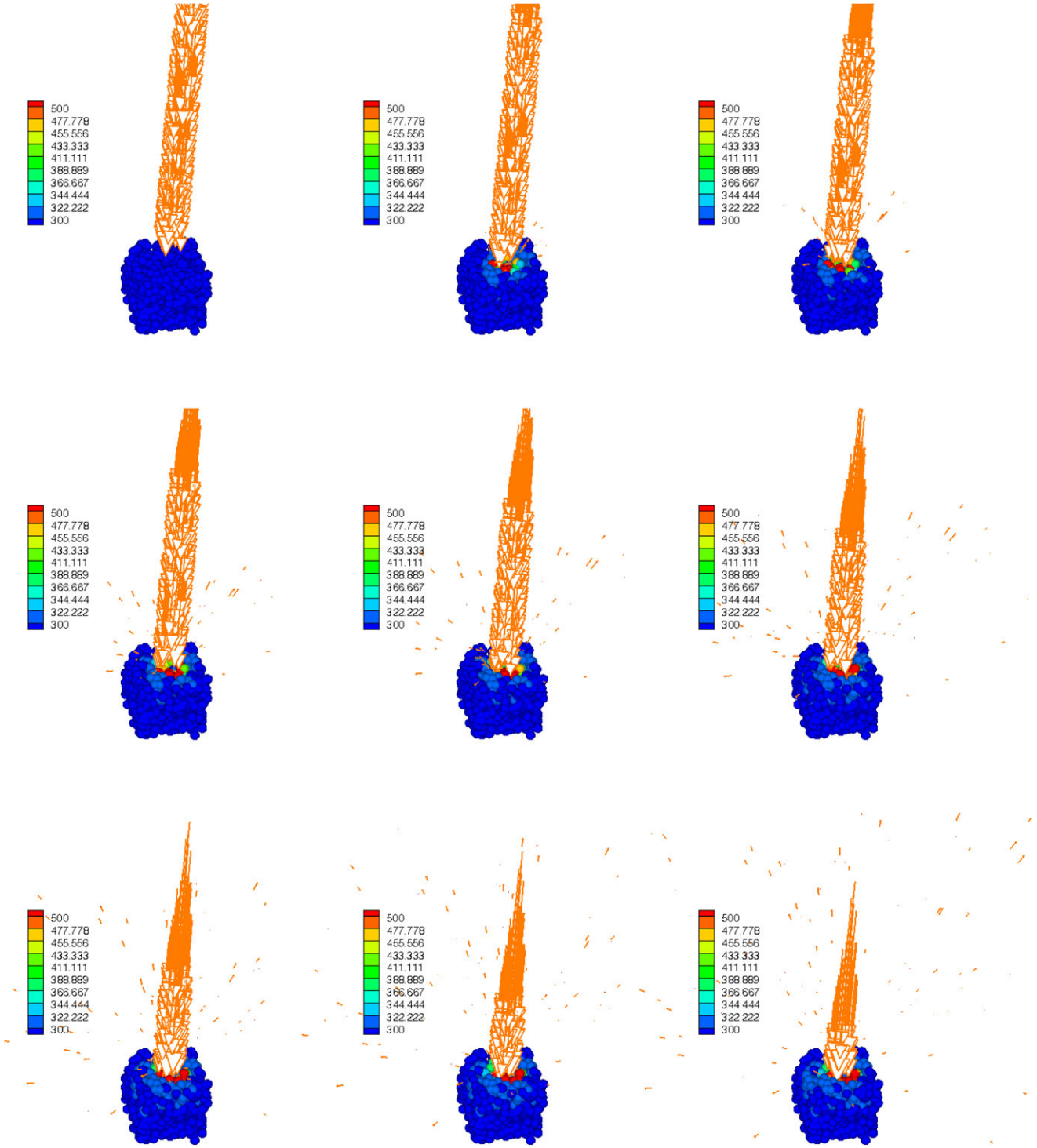

Fig. 8 Frames for the progressive absorption of a Laser beam and subsequent heating for conductivity $\mathbb{K} = 100$

Generally, the deposition of particles to build or enhance components is subclass of additive manufacturing, which in turn is a subfield of advanced manufacturing. Broadly speaking, advanced manufacturing of materials is frequently cited as a blend of techniques from various fields. The "greenness" of an overall process is often considered as a criteria for the approach to be judged as competitive (Dornfeld and Wright [17], Allwood [3], Reich-Weiser, Vijayaraghavan and Dornfeld [41] and Rosen, Dincer and Kanoglu [44]). The true greenness of a combination of techniques which, individually, may be safe and sustainable, is unclear. Take for example, laser ablation of rare earth materials, function-

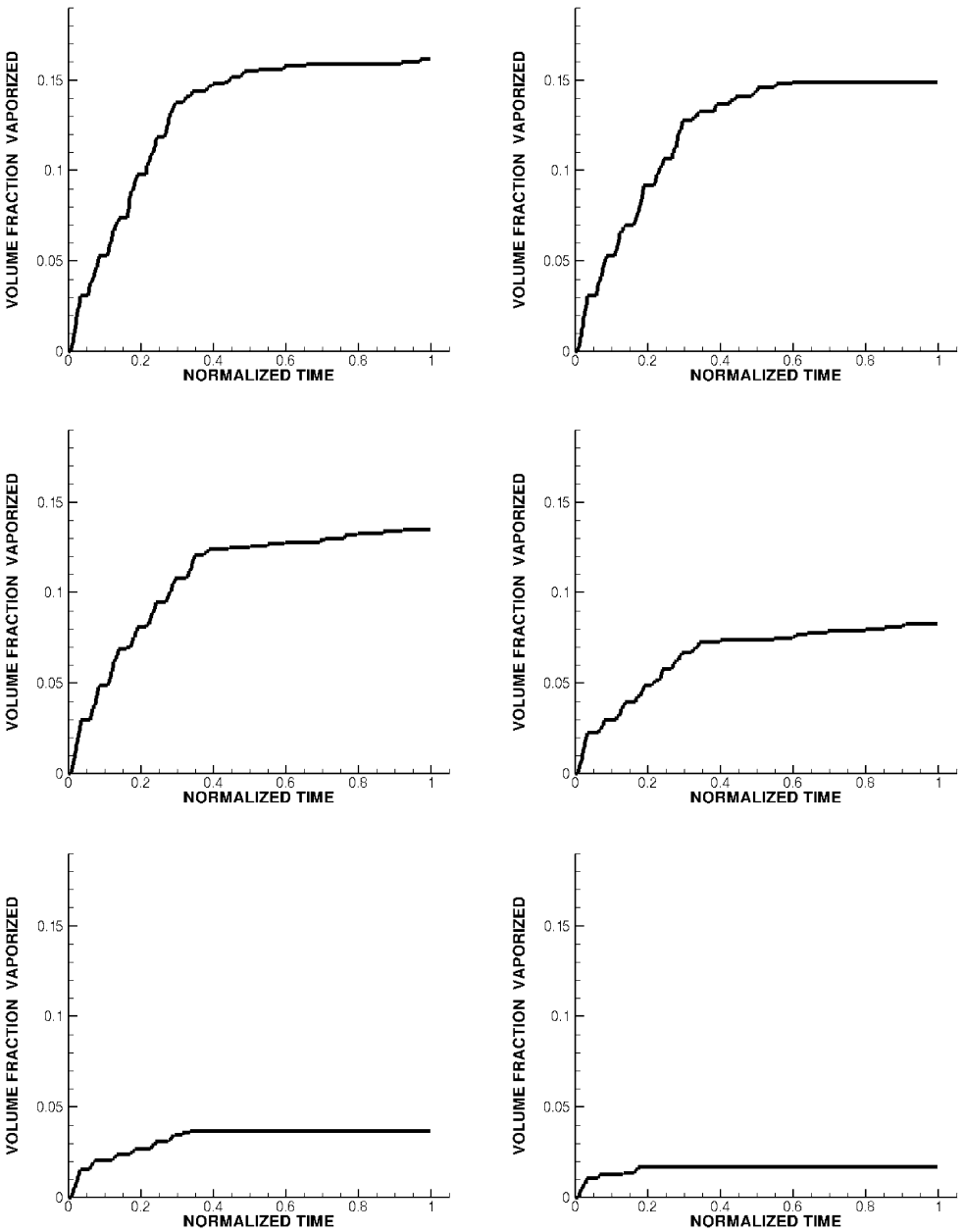

Fig. 9 The volume fraction of vaporized material for $\mathbb{K} = 0$, $\mathbb{K} = 10$, $\mathbb{K} = 20$, $\mathbb{K} = 50$, $\mathbb{K} = 100$ and $\mathbb{K} = 200$

alized inks laden with small-scale particles, etc., which, if done in mass, can produce a highly toxic environment in a non-vacuum processing area. Thus, ablation is of particular interest, due to the potential for dangerous ejecta for large-scale processes. For example, thermal or photothermal ablation usually refers to laser light conversion to lattice vibration before breaking of bonds liberate atomic-scale material, while photochemical/electronic ablation is a direct electronically-induced vibration. Hydrodynamical ablation refers to micrometer droplets following from the molten phase, whereas exfoliation is an erosive mechanism by which material is removed as flakes. Note that all of the mechanisms can occur simultaneously. We refer the reader to the state-of-the-art in Grigoropoulos [21], which categorizes various mechanisms for ablation. A complete model and numerical simulation of this process is currently underway by the author, and is based on methods found in Zohdi [54–59]. This entails an analysis of the dynamics of ablated particulate flows, which are related to granular flow models (see Pöschel and Schwager [40], Duran [18], the works of Torquato and collaborators: Torquato [49], Kansaal et al. [27] and Donev et al. [12–16]) and computational particle methods (see the works of Onate and collaborators: Onate et al. [36, 37], Rojek et al. [43], Carbonell et al. [4] and Labra and Onate [30]).

An overall technological goal is to develop computational tools to accelerate the manufacturing of printed electronics. *Lasers can play a central role in precisely process-*

Table 1 The response sensitivity to a 1000 rays for 1000 randomly dispersed particle scatterers for increasing $\mathbb{K}$ after a sufficiently long time $t = T$, allowing all of the rays to have exited the scattering system ($\mathcal{L} = 0.325$). 20 pulses were applied. In order to adequately compare between different tests, the same random 1000 particle ensemble was used each time

$\mathbb{K}$	Vaporized (v_v)
0	0.162
1	0.159
10	0.149
20	0.135
40	0.095
60	0.071
80	0.040
100	0.037
120	0.022
140	0.020
200	0.017
300	0.008
400	0.006

ing these systems. Print-based methods are ideal for large-scale applications, and provide a framework for assembling electronic circuits by mounting printed electronic devices on flexible plastic substrates, such as polyimide and "PEEK" (Poly-Ether-Ether-Ketone, a flexible thermoplastic polymer) film. There are many variants of this type of technology, which is sometimes referred to as flexible electronics or flex circuits. Flex circuits can be, for example, screen printed silver circuits on polyester.[14] In order to develop flexible microelectronics for large area deployment, traditional methods of fabrication using silicon-based approaches have become limited, due to high cost of materials and equipment (which frequently needs a vacuum environment). For flexibility and lower cost, the ability to develop these electronics on plastics is necessary. Accordingly, print-based technologies are starting to become popular for these applications. In many cases, this requires the development of high volume fraction particle-functionalized "inks". These particles include germanium (which has higher mobility and a more tailorable absorption spectrum for ambient light than silicon) and silver (which is being studied due to the possibility to sinter the particles even without the need high intensity heating). Other semiconductor particle-based materials, including zinc and cadmium based compounds and metals, such as gold and copper, can be considered. Precise patterning of (particle-functionalized) prints is critical for a number of different applications. For recent applications that include low temperature electrode deposition, see Huang et al. [26], for optical coatings and photonics, see Nakanishi et al. [34] and Maier and Atwater [31], for biosensors see Alivisatos [2], for catalysts, see Haruta [24] and for MEMS applications, see Full et al. [20] and Ho et al. [25]. Several methods are available for patterning of particles, such as inkjet printing (see Ridley et al. [42] and Sirringhaus et al. [46]), which is attractive due to its simplicity, high throughput, and low material loss. However, patterning with inkjet printing is limited to a resolution of around 20–50 microns with current printers (Ridley et al. [42]), with higher resolution possible by adding complexity to the substrate prior to printing (Wang et al. [47]). Electrohydrodynamic printing has also been proposed to increase the resolution beyond the limits of inkjet printing, achieving a line resolution as small as 700 nanometers (Park et al. [38]).[15] Unfortunately, inkjet and electrohydrodynamic printing do not allow precise control over the structure of the printed lines. This often results in lines with scalloped edges or non-uniform width, and offer only limited control over the height of the printed features (Huang et al. [26], Sirringhaus et al. [46], Ahmad et al. [1] and Samarasinghe et al. [45]). Also, recently, imprint lithography has been proposed as a means of decreasing the feature size of patterned particles while allowing more precise control over the structure of the printed lines (Ko et al. [28, 29], and Park et al. [39]). In this fabrication method, the particle-laden inks are patterned by pressing with an elastomer mold and the particles are dried into their final configuration. While the resolution of imprint lithography is improved over inkjet printing, there exists a residual layer on the substrate that must be etched away after patterning. Control over the height of features can be corrupted by capillary action between the mold and the drying ink, in particular along the length of longer features. Thus, as a possible alternative to imprint lithography, particle self-assembly methods, based on capillary filling of photoresist templates have been proposed (Demko et al. [10]), and appear to be promising. *Clearly, laser post-processing can play a role in all of the previously mentioned approaches, in order to add a degree of precision that is otherwise missing.*

Appendix: Geometrical Ray Theory

Following a somewhat classical analysis found in, for example, Elmore and Heald [19], Cerveny et al. [8] and others, we consider the propagation of a general disturbance, ψ, governed by a generic wave equation:

$$\nabla^2 \psi = \frac{1}{c^2(\boldsymbol{x})} \frac{\partial^2 \psi}{\partial t^2}. \tag{7.1}$$

Here $c(\boldsymbol{x})$ is a spatially varying wave speed corresponding to a general inhomogeneous medium, where $c(\boldsymbol{x}) = c_o$ in a homogeneous reference medium and where the refractive index is defined as $n = c_o/c(\boldsymbol{x})$. Consider a trial solution of the form

$$\psi(\boldsymbol{x}, t) = A(\boldsymbol{x}) e^{j(k_o S(\boldsymbol{x}) - \omega t)}, \tag{7.2}$$

[14] For an early history of the printed electronics field, see Gamota et al. [23].

[15] In such applications, lasers can be used to heat treat and dry particle-based inks.

where $A(\boldsymbol{x})$ is the amplitude of the disturbance, and where $k_o = \omega/c_o = 2\pi/\lambda$ is the wave number in the reference medium. The function $S(\boldsymbol{x})$ (dimensions of length) is known as the "Eikonal", which in Greek means "image". One can interpret a set of waves as simply a family of surfaces for which the values of $k_o S(\boldsymbol{x})$ differ in increments of 2π. Substituting the trial solution into the wave equation, one obtains

$$k_o^2 A\big(n^2 - \nabla S \cdot \nabla S\big) + jk_o\big(2\nabla A \cdot \nabla S + A\nabla^2 S\big) + \nabla^2 A = 0. \tag{7.3}$$

There are a variety of arguments to motivate so-called "Ray Theory". Probably the simplest is simply to require that, as $k_o \to \infty$, each of the k_o-terms, the zeroth-order k_o-term, the first-order k_o-term and the second-order k_o-term, must vanish. Applying this requirement to the second-order k_o-term yields

$$n^2 = \nabla S \cdot \nabla S = \|\nabla S\|^2. \tag{7.4}$$

For a uniform medium, $n = const$, provided $\nabla^2 A = 0$ and an initial plane wave surface $S = const$, then (7.3) implies

$$S(\boldsymbol{x}) = n(\alpha x + \beta y + \phi z), \tag{7.5}$$

where α, β and ϕ are direction cosines. More generally, when $n \neq 0$, then (7.4) implies

$$\nabla S(\boldsymbol{x}) = n(\boldsymbol{x})\hat{\boldsymbol{s}}(\boldsymbol{x}), \tag{7.6}$$

where $\hat{\boldsymbol{s}}(\boldsymbol{x})$ is a unit (direction) vector. From elementary calculus, recall that ∇S is perpendicular to $S = const$. This allows for the natural definition of continuous curves, called rays, that are everywhere parallel to the local direction $\hat{\boldsymbol{s}}(\boldsymbol{x})$. Rearranging first-order k_o-term of (7.3)

$$\frac{1}{A}\nabla A \cdot \nabla S = -\frac{1}{2}\nabla^2 S = -\frac{1}{2}\nabla \cdot (n\hat{\boldsymbol{s}}). \tag{7.7}$$

Recalling the directional derivative, $\frac{d(\cdot)}{ds} \overset{\text{def}}{=} \hat{\boldsymbol{s}} \cdot \nabla(\cdot)$, we have

$$\left(\frac{\nabla S}{\|\nabla S\|}\right) \cdot \nabla A = \left(\frac{\nabla S}{n}\right) \cdot \nabla A = \frac{dA}{ds}, \tag{7.8}$$

where s is the arc-length coordinate along the ray. With this definition, once $S(\boldsymbol{x})$ is known, the component of ∇A in the $\hat{\boldsymbol{s}}(\boldsymbol{x})$ can be found from (7.7) and (7.8):

$$\frac{1}{A}\frac{dA}{ds} = -\frac{1}{2n}\nabla \cdot (n\hat{\boldsymbol{s}}). \tag{7.9}$$

Thus, we are able to determine how the amplitude of the trial solution changes along a ray, but not perpendicular to the trajectory.

Geometrical "ray-tracing", deals directly with the ray trajectories, rather than finding them as a by-product of the solution of the wave equation for the Eikonal function S and the resulting wave front. To eliminate S we need to look at the rate of change of the quantity $n\hat{\boldsymbol{s}}$ along the ray. Making repeated use of (7.6), we have

$$\begin{aligned}\frac{d(n\hat{\boldsymbol{s}})}{ds} &= \hat{\boldsymbol{s}} \cdot \nabla(\nabla S) = \frac{\nabla S}{n} \cdot \nabla(\nabla S) \\ &= \frac{1}{2n}\nabla(\nabla S \cdot \nabla S) = \frac{1}{2n}\nabla n^2 = \nabla n,\end{aligned} \tag{7.10}$$

where $\frac{d(\cdot)}{ds} \overset{\text{def}}{=} \hat{\boldsymbol{s}} \cdot \nabla(\cdot)$. The previous equation allows us to find the trajectories of a ray ($\hat{\boldsymbol{s}}$), given only the refractive index $n(\boldsymbol{x})$ and the initial direction $\hat{\boldsymbol{s}}_i$ of the desired ray.

Remark A more general derivation of the Eikonal equation can be found in a variety of textbooks, for example, Cerveny et al. [8], and starts by assuming a trial solution of the form

$$\psi(\boldsymbol{x}, t) = A(\boldsymbol{x})\Phi\big(t - \Lambda(\boldsymbol{x})\big) \tag{7.11}$$

where Λ is an Eikonal function, and the waveform function α is assumed to be of high frequency.[16] This function is then substituted into the wave equation to yield

$$\nabla^2 A\Phi + 2\nabla A \cdot \nabla\Phi + A\nabla^2\Phi = \frac{1}{c^2}A\frac{\partial^2\Phi}{\partial t^2}. \tag{7.12}$$

After using the chain rule of differentiation, this can be written as

$$\frac{\partial^2\Phi}{\partial\Lambda^2}A\left(\nabla\Lambda \cdot \nabla\Lambda - \frac{1}{c^2}\right) + \frac{\partial\Phi}{\partial\Lambda}\big(2\nabla A \cdot \nabla\Lambda + A\nabla^2\Lambda\big) + \Phi\nabla^2 A = 0. \tag{7.13}$$

Analogous to the special case considered before, to motivate so-called "Ray Theory" one requires that the coefficients of $\frac{\partial^2\Phi}{\partial\Lambda^2}$, $\frac{\partial\Phi}{\partial\Lambda}$ and Φ are satisfied separately, in other words, the following hold

$$\nabla\Lambda \cdot \nabla\Lambda - \frac{1}{c^2} = 0 \tag{7.14}$$

and

$$2\nabla A \cdot \nabla\Lambda + A\nabla^2\Lambda = 0 \tag{7.15}$$

and

$$\nabla^2 A = 0. \tag{7.16}$$

References

1. Ahmad Z, Rasekh M, Edirisinghe M (2010) Electrohydrodynamic direct writing of biomedical polymers and composites. Macromol Mater Eng 295:315–319
2. Alivisatos P (2004) The use of nanocrystals in biological detection. Nat Biotechnol 22(1):47–52
3. Allwood J (2005) What is sustainable manufacturing? Lecture, Cambridge University
4. Carbonell JM, Onate E, Suarez B (2010) Modeling of ground excavation with the particle finite element method. J Eng Mech 136:455–463

[16] This is a more general case than the one considered in (7.2) where $\Phi(t - \Lambda(\boldsymbol{x})) = e^{j(k_o S(\boldsymbol{x}) - \omega t)}$.

5. Choi S, Park I, Hao Z, Holman HY, Pisano AP, Zohdi TI (2010) Ultra-fast self-assembly of micro-scale particles by open channel flow. Langmuir 26(7):4661–4667
6. Choi S, Stassi S, Pisano AP, Zohdi TI (2010) Coffee-ring effect-based three dimensional patterning of micro, nanoparticle assembly with a single droplet. Langmuir 26(14):11690–11698
7. Choi S, Jamshidi A, Seok TJ, Zohdi TI, Wu MC, Pisano AP (2012) Fast, high-throughput creation of size-tunable micro, nanoparticle clusters via evaporative self-assembly in picoliter-scale droplets of particle suspension. Langmuir 28(6):3102–3111
8. Cerveny V, Molotkov IA, Psencik I (1977) Ray methods in seismology. Univerzita Karlova, Praha
9. Davis SH (2001) Theory of solidification. Cambridge University Press, Cambridge
10. Demko MT, Cheng JC, Pisano AP (2010) High-resolution direct patterning of gold nanoparticles by the microfluidic molding process. Langmuir 26(22):412–417
11. Demko M, Choi S, Zohdi TI, Pisano AP (2012) High resolution patterning of nanoparticles by evaporative self-assembly enabled by in-situ creation and mechanical lift-off of a polymer template. Appl Phys Lett 99:253102
12. Donev A, Cisse I, Sachs D, Variano EA, Stillinger F, Connelly R, Torquato S, Chaikin P (2004) Improving the density of jammed disordered packings using ellipsoids. Science 13(303):990–993
13. Donev A, Stillinger FH, Chaikin PM, Torquato S (2004) Unusually dense crystal ellipsoid packings. Phys Rev Lett 92:255506
14. Donev A, Torquato S, Stillinger F (2005) Neighbor list collision-driven molecular dynamics simulation for nonspherical hard particles. I. Algorithmic details. J Comput Phys 202:737
15. Donev A, Torquato S, Stillinger F (2005) Neighbor list collision-driven molecular dynamics simulation for nonspherical hard particles. II. Application to ellipses and ellipsoids. J Comput Phys 202:765
16. Donev A, Torquato S, Stillinger FH (2005) Pair correlation function characteristics of nearly jammed disordered and ordered hard-sphere packings. Phys Rev E, Stat Nonlinear Soft Matter Phys 71:011105
17. Dornfeld D, Wright P (2007) Technology wedges for implementing green manufacturing. Trans North Am Manuf Res Inst SME 35:193–200
18. Duran J (1997) Sands, powders and grains: an introduction to the physics of granular matter. Springer, Berlin
19. Elmore WC, Heald MA (1985) Physics of waves. Dover, New York
20. Fuller SB, Wilhelm EJ, Jacobson JM (2002) Ink-jet printed nanoparticle microelectromechanical systems. J Microelectromech Syst 11:54–60
21. Grigoropoulos CP (2009) Transport in laser microfabrication. Cambridge University Press, Cambridge
22. Gross H (ed) (2005) Handbook of optical systems: fundamental of technical optics. Wiley-VCH, New York
23. Gamota D, Brazis P, Kalyanasundaram K, Zhang J (2004) Printed organic and molecular electronics. Kluwer Academic, New York
24. Haruta M (2002) Catalysis of gold nanoparticles deposited on metal oxides. CaTTech 6(3):102–115
25. Ho C, Steingart D, Salminent J, Sin W, Rantala T, Evans J, Wright P (2006) Dispenser printed electrochemical capacitors for power management of millimeter scale lithium ion polymer microbatteries for wireless sensors. In: 6th international workshop on micro and nanotechnology for power generation and energy conversion applications (PowerMEMS 2006), Berkeley, CA
26. Huang D, Liao F, Molesa S, Redinger D, Subramanian V (2003) Plastic-compatible low-resistance printable gold nanoparticle conductors for flexible electronics. J Electrochem Soc 150(7):G412–G417
27. Kansaal A, Torquato S, Stillinger F (2002) Diversity of order and densities in jammed hard-particle packings. Phys Rev E, Stat Nonlinear Soft Matter Phys 66:041109
28. Ko SH, Park I, Pan H, Grigoropoulos CP, Pisano AP, Luscombe CK, Frechet JMJ (2007) Direct nanoimprinting of metal nanoparticles for nanoscale electronics fabrication. Nano Lett 7:1869–1877
29. Ko SH, Park I, Pan H, Misra N, Rogers MS, Grigoropoulos CP, Pisano AP (2008) ZnO nanowire network transistor fabrication by low temperature, all inorganic nanoparticle solution process. Appl Phys Lett 92:154102
30. Labra C, Onate E (2009) High-density sphere packing for discrete element method simulations. Commun Numer Methods Eng 25(7):837–849
31. Maier SA, Atwater HA (2005) Plasmonics: localization and guiding of electromagnetic energy in metal/dielectric structures. J Appl Phys 2005:98, 011101
32. Martin P (2009) Handbook of deposition technologies for films and coatings, 3rd edn. Elsevier, Amsterdam
33. Martin P (2011) Introduction to surface engineering and functionally engineered materials. Scrivener and Elsevier, Amsterdam
34. Nakanishi H, Bishop KJM, Kowalczyk B, Nitzan A, Weiss EA, Tretiakov KV, Apodaca MM, Klajn R, Stoddart JF, Grzybowski BA (2009) Photoconductance and inverse photoconductance in thin films of functionalized metal nanoparticles. Nature 2009(460):371–375
35. Niemz MH (2004) Laser tissue interactions-fundamentals and applications. Springer, Berlin
36. Onate E, Idelsohn SR, Celigueta MA, Rossi R (2008) Comput Methods Appl Mech Eng 197(19–20):1777–1800
37. Onate E, Celigueta MA, Idelsohn SR, Salazar F, Surez B (2011) Possibilities of the particle finite element method for fluid-soil-structure interaction problems. Comput Mech 48:307–318
38. Park J-U, Hardy M, Kang SJ, Barton K, Adair K, Mukhopadhyay DK, Lee CY, Strano MS, Alleyne AG, Georgiadis JG, Ferreira PM, Rogers JA (2007) High-resolution electrohydrodynamic jet printing. Nat Mater 6:782–789
39. Park I, Ko SH, Pan H, Grigoropoulos CP, Pisano AP, Frechet JMJ, Lee ES, Jeong JH (2008) Nanoscale patterning and electronics on flexible substrate by direct nanoimprinting of metallic nanoparticles. Adv Mater 20:489
40. Pöschel T, Schwager T (2004) Computational granular dynamics. Springer, Berlin
41. Reich-Weiser C, Vijayaraghavan A, Dornfeld DA (2008) Metrics for manufacturing sustainability. In: Proc IMSEC, ASME, Evanston, IL, October 7–10
42. Ridley BA, Nivi B, Jacobson JM (1999) All-inorganic field effect transistors fabricated by printing. Science 286:746–749
43. Rojek J, Labra C, Su O, Onate E (2012) Comparative study of different discrete element models and evaluation of equivalent micromechanical parameters. Int J Solids Struct 49:1497–1517. doi:10.1016/j.ijsolstr.2012.02.032
44. Rosen M, Dincer I, Kanoglu M (2008) Role of energy in increasing efficiency and sustainability and reducing environmental impact. Energy Policy 36:128–137
45. Samarasinghe SR, Pastoriza-Santos I, Edirisinghe MJ, Reece MJ, Liz-Marzan LM (2006) Printing gold nanoparticles with an electrohydrodynamic direct write device. Gold Bull 39:48–53
46. Sirringhaus H, Kawase T, Friend RH, Shimoda T, Inbasekaran M, Wu W, Woo EP (2000) High-resolution inkjet printing of all-polymer transistor circuits. Science 290:2123–2126
47. Wang JZ, Zheng ZH, Li HW, Huck WTS, Sirringhaus H (2004) Dewetting of conducting polymer inkjet droplets on patterned surfaces. Nat Mater 3:171–176
48. Steen WM (1998) Laser material processing. Springer, Berlin
49. Torquato S (2002) Random heterogeneous materials: microstructure & macroscopic properties. Springer, New York

50. Zohdi TI (2006) On the optical thickness of disordered particulate media. Mech Mater 38:969–981
51. Zohdi TI (2006) Computation of the coupled thermo-optical scattering properties of random particulate systems. Comput Methods Appl Mech Eng 195:5813–5830
52. Zohdi TI, Kuypers FA (2006) Modeling and rapid simulation of multiple red blood cell light scattering. J R Soc Interface 3(11):823–831
53. Zohdi TI (2012) Electromagnetic properties of multiphase dielectrics: a primer on modeling, theory and computation. Springer, Berlin
54. Zohdi TI (2004) A computational framework for agglomeration in thermo-chemically reacting granular flows. J R Soc Interface 460(2052):3421–3445
55. Zohdi TI (2005) Charge-induced clustering in multifield particulate flow. Int J Numer Methods Eng 62(7):870–898
56. Zohdi TI (2007) Computation of strongly coupled multifield interaction in particle-fluid systems. Comput Methods Appl Mech Eng 196:3927–3950
57. Zohdi TI (2010) On the dynamics of charged electromagnetic particulate jets. Arch Comput Methods Eng 17(2):109–135
58. Zohdi TI (2012) Dynamics of charged particulate systems: modeling, theory and computation. Springer, Berlin
59. Zohdi TI (2013) Numerical simulation of charged particulate cluster-droplet impact on electrified surfaces. J Comput Phys 233:509–526